

Near-field dynamics of a turbulent round jet with moderate swirl

Y. Maciel ^{a,*}, L. Facciolo ^b, C. Duwig ^{c,d}, L. Fuchs ^{b,c}, P.H. Alfredsson ^b

^a Department of Mechanical Engineering, Laval University, Quebec City, Canada G1V 0A6

^b Linné Flow Centre, KTH Mechanics, Royal Institute of Technology, SE-100 44 Stockholm, Sweden

^c Division of Fluid Mechanics, Department Energy Sciences, Lund University Box 118, SE- 22100 Lund, Sweden

^d Haldor Topsoe A/S, DK-2800 Lyngby, Denmark

Received 9 November 2007; received in revised form 1 February 2008; accepted 9 February 2008

Available online 28 March 2008

Abstract

The near-field characteristics of a turbulent jet with moderate swirl generated by a fully developed, axially rotating pipe flow are investigated with LDV, time-resolved stereoscopic PIV measurements, as well as with large-eddy simulations. Large-scale vortical structures in either double, triple or even quadruple-helix configuration are found at the pipe exit but rapidly break down or amalgamate after two jet diameters. Further downstream, the swirling jet is dominated by large-scale sweeping motions not present at such a scale and strength in the non-swirling case. Of special interest is the recently discovered counter-rotating core (in the mean) which develops about six jet diameters downstream the jet exit. Data for all six Reynolds stresses is reported at this position and it is argued that the counter-rotation is the result of the transport of angular momentum radially outward by the radial–azimuthal Reynolds shear stress. The mechanisms behind this transport are discussed by qualitative analysis of the time-resolved PIV and LES data and comparisons with the non-swirling case are made.

© 2008 Elsevier Inc. All rights reserved.

Keywords: Swirling jet; Turbulence; LDV; Stereoscopic PIV; Time-resolved PIV; LES

1. Introduction

In a turbulent jet, the presence of swirl may strongly affect the mean flow features. At moderate swirl numbers, the turbulence and spreading of the jet increase. At swirl ratios above a critical level so called vortex breakdown occurs which changes the jet behaviour completely. In the following we will limit ourselves to moderate swirl for which vortex breakdown does not occur. A swirling round jet is axisymmetric on average but the swirl breaks the symmetry, which means for instance that the two Reynolds shear stresses which involve the fluctuating azimuthal component are non-zero in contrast to the non-swirling case.

Crow and Champagne (1971) were among the first to recognize that the large-scale coherent structures found in the near-field of round jets are strongly related to the shear layer

instabilities. In non-swirling jets, axisymmetric vortex rings are initially formed close to the nozzle exit but helical disturbances may appear further downstream. According to the linear stability theory (Michalke, 1984), helical instability waves of azimuthal wavenumber $m = 1$ (in a modal decomposition of the form $\exp[i(kx + m\theta + \omega t)]$) become more unstable than the axisymmetric mode $m = 0$ when the shear layer is thick. In their low-Reynolds-number experiments, Dimotakis et al. (1983) found large-scale vortical structures that are either nearly axisymmetric, or spiral, or in a transitional state between these two configurations. The jet switches back and forth between these different states. At the highest Reynolds numbers ($Re \approx 10,000$), they found that the dominant mode after one or two jet diameters was the helical one. Other experiments have also revealed helical components appearing close to the nozzle exit at high Reynolds numbers (Ho and Huerre, 1984).

From the above discussion, it is expected that the structure of the near-field turbulence should be distinctly

* Corresponding author. Tel.: +1 418 656 7967; fax: +1 418 656 7415.
E-mail address: yvan.maciel@gmc.ulaval.ca (Y. Maciel).

different between a jet exiting from a smooth contraction nozzle with a thin laminar shear layer and a jet exiting from a long pipe with a fully developed turbulent pipe flow profile. In the case of the pipe jet flow, the regular formation of vortex rings resulting from the shear layer instability was found to be disrupted by turbulent exit conditions (Mi et al., 2001; Xu and Antonia, 2002). Xu and Antonia (2002) showed that the initially thicker shear layer in the case of the pipe jet flow results in longer wavelength primary instabilities and structures. Mi et al. (2001) provide some evidence that the formation of large-scale structures in the pipe jet occurs much farther downstream (around six jet diameters) than in the contraction jet (around one jet diameter).

The situation becomes even more complicated in a swirling jet since the flow is more complex and the initial conditions are even more diverse. For instance, in addition to its three-dimensional character, the jet shear layer is subjected to centrifugal effects because of its azimuthal velocity component. The effect of swirl (below the onset of vortex breakdown) on the development of jet instabilities and coherent structures has been considered in a few studies. Martin and Meiburg (1994) determined the inviscid linear instability properties of a family of swirling jet models. It was found that when the flow is centrifugally unstable (rapid decrease of circulation away from the jet axis), the most unstable modes were the positive helical modes ($m > 0$). Panda and McLaughlin (1994) studied experimentally the instability waves and the resulting organized structures in a jet with high swirl levels (close to breakdown) in the Reynolds number range 20,000–60,000. The swirling jets showed only weak and very irregular large-scale structures in the shear layer. However, acoustic excitation produced regular organized structures in both helical ($m = +1$ and -1) and axisymmetric modes. They concluded that swirl tends to reduce the amplification of the unstable modes.

Loiseleur and Chomaz (2003) made a detailed experimental analysis on the instability of swirling jets at low-Reynolds-number ($Re = 740$ and 1490). They found three distinct dynamical flow regimes for swirl numbers below that for which vortex breakdown occurs. For small swirl numbers, the flow was found to be governed by the same axisymmetric instability mechanism as in the non-swirling case. As the swirl number increased, the amplitude of the axisymmetric mode decreased and instead a helical mode grew, of gradually decreasing wavenumber from $m = 7$ to 4. Traveling anticyclonic co-rotating streamwise vortices were formed in the braids connecting vortex rings. In the intermediate swirl range, vortex rings formed concurrently with several interacting helical cyclonic waves of azimuthal wavenumber $m = 2$. The shape of the jet became distorted into a double-helix due to the roll-up action of the shear in the azimuthal direction. In the high swirl regime immediately preceding vortex breakdown, although vortex rings still persisted, the dominant mode was $m = 1$. It propagated anticyclonically but its appearance was sporadic and localized.

On the numerical side, Martin and Meiburg (1998) used a vortex filament technique to perform a numerical simulation of the inviscid vorticity dynamics in a simplified swirling jet model, the same model as in Martin and Meiburg (1994). Hu et al. (2001) used DNS to study a temporally evolving jet under axisymmetric and azimuthal disturbances. McIlwain and Pollard (2002) studied the interaction between coherent structures in non-swirling and mildly swirling jets with LES ($Re = 68,000$). They found skewed vortex rings. The addition of swirl increased the number of streamwise braids which apparently enhanced the breakdown mechanism of the rings.

In addition to the intrinsic flow complexity, the study of swirling jets is further complicated by the fact that the initial conditions can be extremely diverse. Many swirling-generating mechanisms can be used, such as guide vanes, rotating honeycombs, transverse injection and so on, leading to various axial and azimuthal velocity distributions. The resulting flow is to a certain extent dependent on the geometrical details of the apparatus, which makes comparisons between various studies difficult. One method to get an apparatus-independent swirl is to use an axially rotating, fully developed pipe flow as the source for the swirling jet. Such a pipe flow apparatus was developed by Facciolo (2006). However it was discovered (Facciolo et al., 2007) that the resulting swirling jet flow has a puzzling characteristic, namely that at approximately six pipe diameters downstream of the pipe outlet, the jet core starts to rotate in the mean (albeit at a low rate) in the opposite direction as compared to the rotation of the pipe. Our aim in this paper is to further investigate this behaviour, together with the overall near-field dynamics of the jet, using LDV and time-resolved stereoscopic PIV measurements, as well as LES simulations.

2. Methods of investigation

2.1. Pipe flow apparatus

The jet flow is generated from a fully developed turbulent pipe flow for both the swirling and non-swirling cases. The pipe is mounted horizontally and has a length of 6 m and a diameter D of 60 mm. The pipe can be rotated along its axis with a maximum rotation rate of 30 rev/s. The flow is entering the ambient still air through a large non-rotating plate (for more details see Facciolo, 2006).

A laboratory-fixed cylindrical reference frame is used to describe the flow. We denote the radial, azimuthal and axial directions by r , θ and x with the origin of the coordinate system at the center of the pipe outlet. The corresponding velocity components are u_r , u_θ and u , respectively. For convenience, a cartesian reference frame is also defined with y in the horizontal direction and z in the vertical direction, and corresponding velocity components v and w .

2.2. LDV systems

Two different LDV systems were used. The first one is a FlowLite system from DANTEC used to measure the streamwise and azimuthal velocity components separately. The system comprised of a backscatter fibre optics probe with a beam expander, a Bragg cell and a signal analyser of correlation type. The light source was a 10 mW He–Ne laser. The measuring volume, an ellipsoid, had the dimensions: $0.81 \times 0.09 \times 0.09 \text{ mm}^3$. The data rate varied depending on the measurement position with the highest rate in the central region. To acquire statistically independent samples the sampling rate was limited to 100 Hz (estimated as U_b/D , where U_b is the bulk velocity in the pipe and D is the pipe inner diameter). The sampling was stopped either at 12,000 samples or after 240 s.

The second LDV system, an Aerometric optical system, was used to measure the radial and azimuthal components. Here an Argon laser, with wave lengths of 488 and 514 nm, together with Bragg cells, was used. The signals were analyzed using a two channel BSA Flow system from DANTEC. The optical axes of the LDV probes are perpendicular to each other to allow simultaneous measurements of the radial and azimuthal velocity components. In order to minimize the probe volume (which for each probe is similar to the one of the FlowLite system), the scattered light was picked up by the probe head at 90° to the one emitting the light, thereby effectively reducing the probe volume to a sphere with a diameter of 0.1 mm. Data were only acquired when simultaneous signals were coming from both probes showing that the same particle is giving rise to both signals. For this set of measurements, the number of independent samples was typically around 20,000.

The particles used for the LDV measurements are small droplets of condensed smoke of polyethylenglycol. They are injected into the air at the inlet of the centrifugal fan.

2.3. PIV system

The stereoscopic PIV system consists of two high-speed digital cameras Photron Fastcam APX RS, CMOS sensor, which can catch images up to 250 kHz, and a dual-head, high-repetition-rate, diode-pumped Nd:YLF laser Pegasus PIV by New Wave with a maximum frequency of 10 kHz. During the experiments the image pairs are captured at a frequency of 1.5 kHz with a resolution of 1024×1024 pixels at 10 bit using Nikon Nikkor 105 mm lenses. Two types of datasets were obtained. The first one corresponds to measurements over a long time period ($1.4 \times 10^4 D/U_b$) in order to perform statistics with statistically independent velocity field realizations (generally 3696 realizations). The second type consists in time-resolved measurements with a temporal resolution of $0.077D/U_b$ and typically 3072 realizations. For both types of datasets, the spatial resolution is approximately $0.015D$.

A commercial software from La Vision (Davis 7.0) has been used for the stereoscopic calibration and the processing of the images. In stereo PIV, important systematic errors can be introduced by slight misalignments of the laser sheet with respect to the calibration plane. These errors were reduced by applying a self-calibration procedure available in Davis 7.0. The remaining systematic errors were still too large in relative terms for the components v and w in the yz -planes. In order to have reliable strain and rotation rates when analysing the instantaneous velocity fields, a procedure was used to correct the remaining systematic errors for the components v , w , u_r and u_θ by using the LDV mean data as reference data. The fields are also corrected for small geometric misalignment errors of the measurement plane. A two-dimensional homogeneous Gaussian filter is finally used to smooth the raw instantaneous PIV velocity fields. The size of the spatial filtering window is 5×5 grid points.

The seeding used for the PIV is the same as for the LDV, with the difference that the droplets of polyethylenglycol are generated by an atomiser which makes them larger and thereby peak locking problems in the images are avoided.

2.4. Large-eddy simulations

In the LES framework, we consider the continuity and Navier–Stokes equations where the dependent variables are decomposed into resolved and unresolved (or subgrid) components using spatial filtering of length Δ :

$$\nabla \cdot \bar{u} = 0 \quad (1)$$

$$\frac{\partial \bar{u}}{\partial t} + \bar{u} \cdot \nabla \bar{u} = -\nabla \bar{p} + \nabla \cdot (\bar{u}\bar{u} - \bar{u}\bar{u} + v\nabla \bar{u}) \quad (2)$$

where u is the velocity vector, p the pressure divided by the reference density, v the kinematic viscosity and the overbar denotes the filtered (resolved) components. One needs to introduce closure models for the subgrid stress terms arising in Eq. (2). The closure model employed in this paper is of classical gradient type with an effective ‘eddy’ viscosity, $v_\Delta = C\Delta\sqrt{\bar{F}_2}$, modeled by the Filtered Structure Function Model (FSFM) (Ducros et al., 1996), where $\bar{F}_2 = [\|\text{HP}(\bar{u}(\mathbf{x}, t) - \bar{u}(\mathbf{x} + \mathbf{r}, t))\|^2]_{\|\mathbf{r}\|=\Delta}$ is the filtered second order velocity structure function. HP denotes a high-pass filter and C is a model constant (Ducros et al., 1996). This model was successfully used in the study of similar problems (e.g. da Silva and Métais, 2002). Several other models are available in the literature (Sagaut, 2001) but will not be discussed here.

The boundary conditions and particularly the inlet conditions are important in the framework of large-eddy simulations. In order to obtain fully developed swirling pipe flow conditions at the inlet, one may want to start the computation far upstream from the region of interest (long pipe) or, alternatively, generate the inflow conditions with a separate LES or DNS of the fully developed swirling pipe

flow. These two approaches are however computationally very expensive and demanding. Instead, it was decided to use a compromise that ensures that the modeling of the inflow boundary gives a reasonable approximation to the experimental set-up. The LES computation therefore starts at the end of the pipe. For any variable u , the inflow boundary is obtained as a weighted average of the jet and coflow values. Thus,

$$u(x = 0, r, \theta, t) = (1 - \gamma)u_{\text{jet}}(r, \theta, t) + \gamma u_{\text{coflow}} \quad (3)$$

with

$$\gamma = 0.5 + 0.5 \tanh((r - D/2)/\delta) \quad (4)$$

The thickness δ is taken to be $D/20$ which is commonly used for LES of turbulent jet (da Silva and Métais, 2002). Entrainment of the surrounding fluid is made possible by using a low velocity constant coflow with $u_{\text{coflow}} = 0.05U_b$ as recommended by da Silva and Métais (2002). For the jet, the time dependent inlet velocity is imposed such that

$$u_{\text{jet}}(r, \theta, t) = u_{\text{mean}}(r) + F(u_{\text{rms}}(r), y, z, t) \quad (5)$$

where u_{mean} and u_{rms} are taken from the experimental LDV database. A seemingly turbulent fluctuation is given by the function F . F was generated using the digital filter technique of Klein et al. (2003) as function of the local Reynolds stress components and the local turbulent characteristic length scales. These quantities were obtained from the experimental database of Facciolo (2006) assuming a non-swirling fully developed pipe flow. This digital filter approach was used successfully in LES and DNS simulations of various turbulent flows (Klein et al., 2003; Ahlman et al., 2007; Duwig and Fureby, 2007; Duwig et al., 2008). It would fail if strong, large-scale coherent structures of the type encountered in the jet shear layer were also present in the pipe but this is not the case. As suggested by the turbulence statistics (Facciolo et al., 2007; Facciolo, 2006), the large-scale structures present in the swirling pipe flow should not differ considerably from those of the non-swirling pipe flow. They are therefore much less energetic and less regularly formed than the large-scale structures generated in the jet shear layer. The fact that they are not modeled in detail but rather statistically approximated should not affect significantly the instability mechanisms and the overall jet development. The digital filter based approach is therefore believed to be adequate in the present case. At the outlet, all variables are assumed to have a zero gradient with a correction ensuring mass conservation.

The LES code is a high-order finite difference Cartesian code that solves the incompressible Navier–Stokes equations on Cartesian grids (Gullbrand et al., 2001). The spatial discretization is done using a fourth order centered scheme. Stability is ensured by including a hyper-viscosity type term. A second order finite difference scheme is used for time discretization and the time integration is done implicitly. Multi-grid iterations are used to solve the implicit parts of the system and local refinements are used to

capture high gradients. The use of finite differences is well suited for LES of turbulent jets providing accurate and fast results, e.g. Duwig et al. (2007), Olsson and Fuchs (1996). More details about the code can be found in Gullbrand et al. (2001).

The computational domain consists of a box of size $24D \times 8D \times 8D$ starting at the exit of the rotating pipe. Two computational grids are used with, respectively, 1.8 (coarse grid) and 3.8 (fine grid) millions nodes. The grid is refined toward the jet location with an averaged mesh size of $D/32$ (coarse grid) and $D/40$ (fine grid) close to the jet nozzle. Therefore, the LES cut-off filter is of the order of the Taylor micro-scale and falls well into the inertial subrange of the turbulent spectrum indicating that the present grids are adequate for performing simulations. In addition, the present spatial resolution is well in line with previous simulations of turbulent jets, e.g. Olsson and Fuchs (1996), da Silva and Métais (2002). The time step is chosen to keep the inlet CFL (Courant–Friedrich–Levy number) below 0.3. The time averaging operation has been performed over 80,000 time steps corresponding to ≈ 750 time units τ with $\tau = D/U_b$.

3. Results and discussion

All the data presented here is for $Re = U_b D / v \approx 24,000$ and swirl numbers of $S = 0$ and $S \approx 0.5$ ($S = 0.43, 0.47$ and 0.5 for PIV, LDV and LES, respectively). Note that LDV and LES data are only available for the swirling case, with the exception of axial velocity data also obtained with LDV in the non-swirling case. Furthermore, PIV data is only available at $x/D = 6$. The swirl number is defined as $S = V_w/U_b$ where V_w is the azimuthal velocity of the inner pipe wall. Comparisons between the LDV, PIV and LES data are presented whenever possible. The PIV profiles shown here were all obtained by averaging the data of the planar fields in the azimuthal direction.

3.1. Mean velocity

The LDV and LES data are used first to present the streamwise evolution of the mean flow characteristics. The mean axial velocity profiles at three streamwise positions with and without swirl are shown in Fig. 1. The initial profile at the pipe outlet is more peaked for the swirling flow case. However, further downstream at $x/D = 6$ the axial velocity in the central region becomes smaller than in the non-rotating case. At the latter position, it is seen that the LDV and PIV data agree very well. The LES mean axial velocity results (Fig. 1b) reproduce the jet expansion rate but overestimate the decay rate of the axial velocity along the centerline (centerline velocity underestimated by 9% at $x/D = 6$). This discrepancy may be due in part to slightly different inflow conditions, both in terms of mean flow and turbulence, and probably to a less extent to different lateral boundary conditions and coflow. The initial development of a turbulent round jet is known to

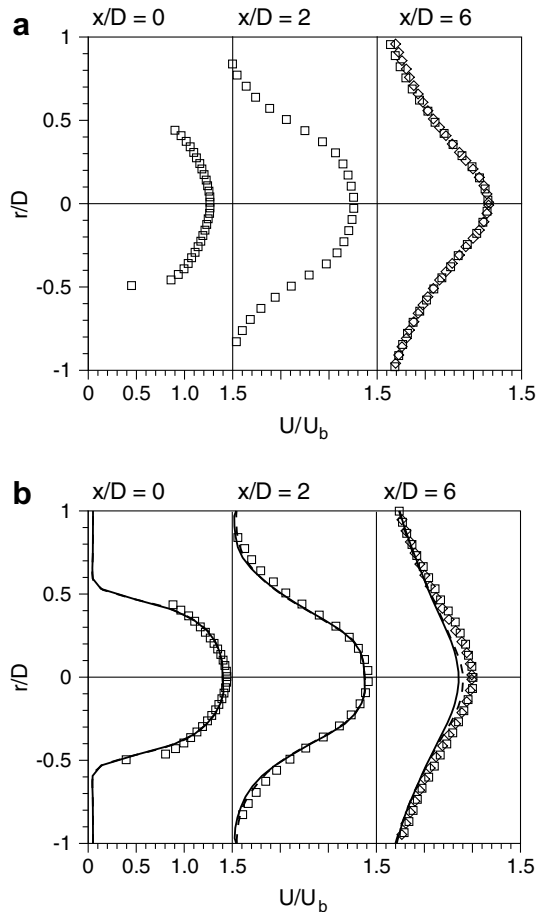


Fig. 1. Mean axial velocity profiles for (a) $S = 0$ and (b) $S \approx 0.5$. \square , LDV; \diamond , PIV; —, LES coarse grid; --, LES fine grid.

be sensitive to even relatively small changes in the inflow conditions as has been shown for instance by Russ and Strykowski (1994). Differences in the centerline velocity of the same order as those obtained here have been reported before when DNS or LES results of turbulent round jets are compared with experimental results (Olsson and Fuchs, 1996; Boersma et al., 1998). Note that even experimental data sets of turbulent round jets having sup-

posedly the same inflow conditions tend to show scatter of the same order when they are compared (Olsson and Fuchs, 1996; Boersma et al., 1998), scatter which cannot solely be attributed to experimental errors.

Fig. 1b also shows the results of the LES computations performed on two different grids. The difference between the two sets of data is generally below the experimental uncertainty and not significant. The same is seen comparing other velocity components and higher moments (not presented here) indicating that the grid resolution is adequate and that refining further the grid would not change the results in terms of mean velocity and Reynolds stresses.

Fig. 2 shows the downstream evolution of the mean azimuthal velocity profiles (U_θ/U_b) for the swirling jet. The velocity profile at the pipe outlet closely follows a profile proportional to $(r/R)^2$. The mean flow field of the upstream rotating pipe flow deviates from solid body rotation due to radial turbulent transport of azimuthal momentum. From the figure it is seen that the maximum of U_θ decreases to almost 50% of the pipe wall velocity V_w (25% of U_b , $V_w \approx 0.5U_b$) in only one diameter, due to the entrainment of ambient fluid. At $x/D = 8$, the maximum of U_θ is reduced to about 10% of V_w and is shifted to $r/D \approx 1$.

Fig. 3 shows a close-up of the profiles in the central region of the jet from $x/D = 5$ to 8. Starting at $x/D = 6$, the profiles reveal a change in sign meaning that in average the jet, in the central region, rotates in a direction which is opposite to that imposed by the rotating pipe. The azimuthal velocity of the counter-rotating core is fairly small, about 1% of V_w , and it covers a region slightly smaller than the pipe diameter. The counter-rotating region starts between 5D and 6D downstream of the pipe outlet, increasing in magnitude and reaching a maximum between 6D and 8D.

The comparisons in Figs. 2 and 3 between the PIV and LDV U_θ -profiles at $x/D = 6$ reveals a fairly good agreement. Note however that such an agreement is reached only when the PIV data is averaged over the azimuthal direction. Relatively large systematic errors of U_r and U_θ exist for the PIV data due to the misalignment problems

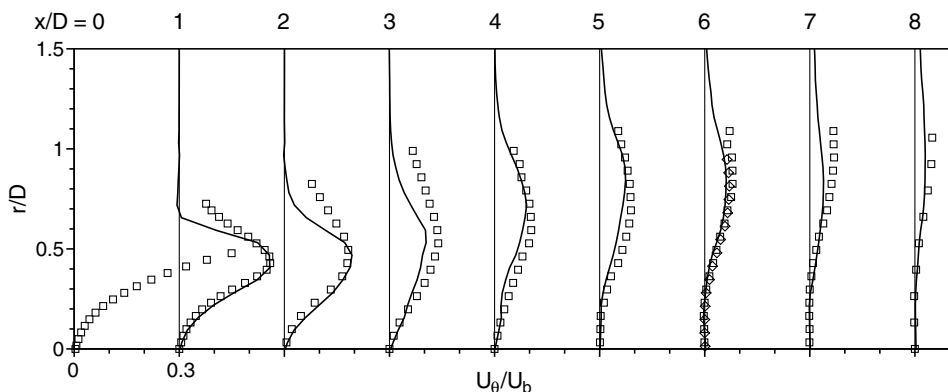


Fig. 2. Mean azimuthal velocity profiles of the swirling jet. \square , LDV; \diamond , PIV, $x/D = 6$ only; —, LES. Not all data points shown for clarity.

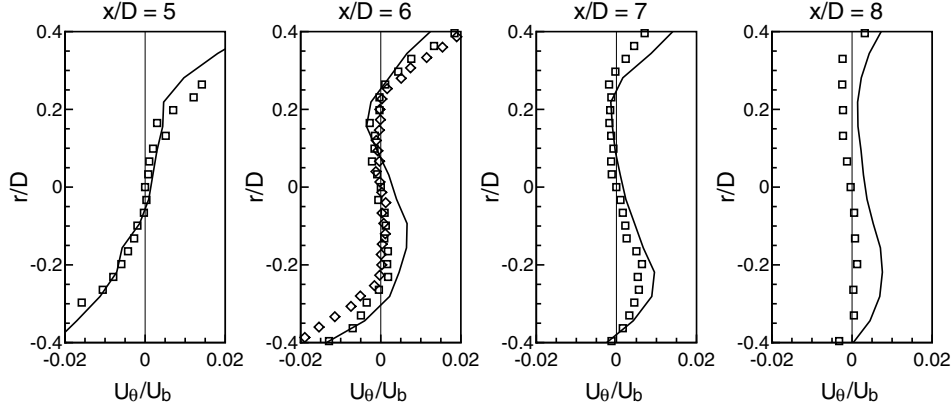


Fig. 3. Mean azimuthal velocity profiles of the swirling jet. Close-up of the jet core. Symbols and lines as in Fig. 2.

described in the previous section. Since U_r and U_θ are very small at $x/D = 6$, the errors reach $\pm 30\%$ of its maximum value for U_θ and $\pm 100\%$ of its maximum value for U_r . As mentioned previously, a procedure was used to correct the PIV instantaneous velocity data for these systematic errors. Fig. 2 shows that for $x/D < 4$, the agreement between LES and experimental data is good for $r/D < 0.5$ but the LES tends to underestimate the azimuthal velocity in the outer part of the jet. Further downstream, the three data sets of U_θ agree well. It can be deduced from Fig. 2 that the flux of angular momentum is smaller in the simulation. Nonetheless, from Figs. 1 and 2 we conclude that the LES simulation represents fairly well the swirling jet mean flow features.

3.2. Reynolds stresses

Fig. 4 shows the radial distribution of the Reynolds normal stresses at $x/D = 6$ for both non-swirling and swirling cases. For all stresses the level is higher in the swirling case (typically 50–100% higher values) as compared to the non-swirling case. In the swirling case we can note that the stresses in the core region are fairly constant, whereas for the non-rotating case the stresses have a maximum around $r/D = 0.4$. We can also note that there is a good correspondence between the LDV and the PIV data. The LES seems to underestimate $\overline{u^2}$ and the shape of the profiles are slightly different for the other two normal stresses. But overall, the LES results present a reasonable agreement with the experimental data predicting the shape and magnitude of the normal stresses.

In axisymmetric non-swirling jets, only one of the Reynolds shear stresses, namely $\overline{u'u_r}$, is different from zero, whereas the other two stresses are zero due to symmetry. In Fig. 5 all the Reynolds shear stresses are shown (except those which are zero by definition). Also here it is clear that in the non-swirling case, the $\overline{u'u_r}$ stress is at a lower level than for the swirling case. More interesting is to see the distribution of the two other stresses which both are positive. An interesting feature is the local maximum of $\overline{u'u_r}$ around

$r/D = 0.25$. The comparison for $\overline{u'_\theta u'_r}$ between the PIV and the LDV measurements, the only one available, is again convincing. The comparison for $\overline{u'u'_r}$ between the PIV and the LES data is reasonably good. The LES data for the

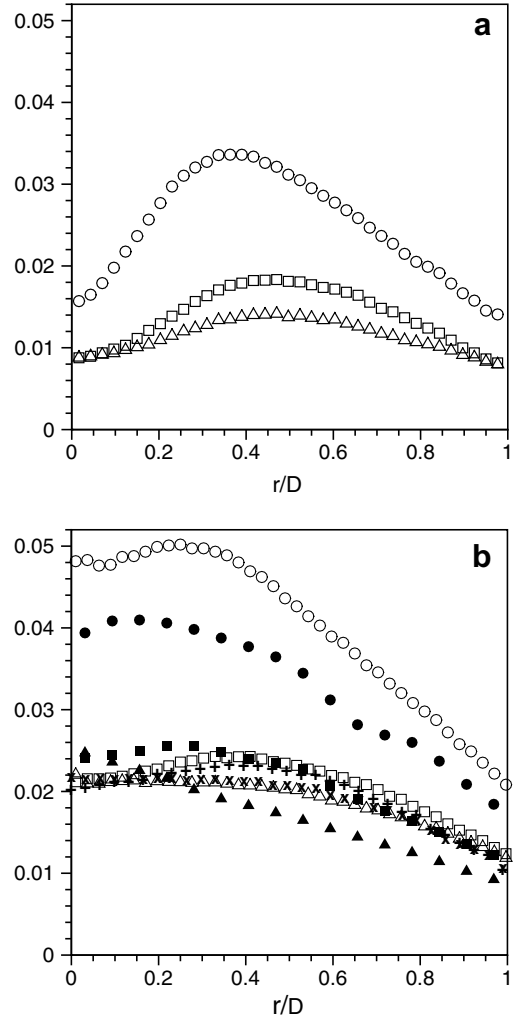


Fig. 4. Reynolds normal stress profiles at $x/D = 6$ normalized with U_b^2 for (a) $S = 0$ and (b) $S \approx 0.5$: \circ , $\overline{u^2}$; \square , $\overline{u_\theta^2}$; \triangle , $\overline{u_r^2}$. PIV: open symbols, LES: filled symbols. LDV, $S = 0.47$: $+$, $\overline{u_\theta^2}$; \times , $\overline{u_r^2}$.

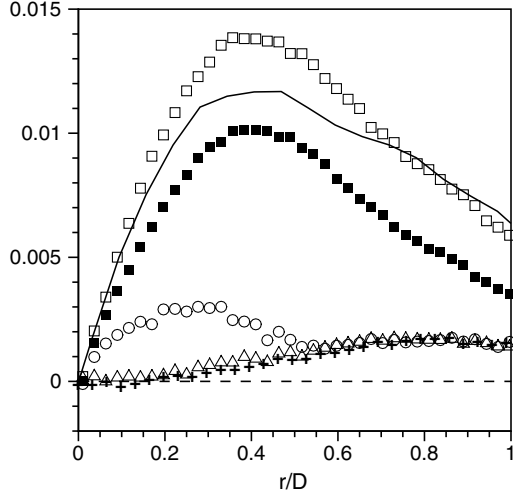


Fig. 5. Reynolds shear stress profiles at $x/D = 6$ normalized with U_b^2 . PIV: \circ , $u' u'_\theta$; \square , $u' u'_r$; \triangle , $u'_\theta u'_r$; open symbols $S = 0.43$, filled symbols $S = 0$. LDV, $S = 0.47$; $+$, $u'_\theta u'_r$. LES, $S \approx 0.5$: $—$, $u' u'_r$.

other two shear stresses is not shown because the relative uncertainties are too large due to a lack of statistically independent realizations.

3.3. Mean angular momentum

It is possible to formulate an approximate conservation equation for the axial flux of angular momentum which states

$$\frac{d}{dx} \int_0^\infty \rho (U\Gamma + r\overline{u' u_\theta}) 2\pi r dr = 0$$

where ρ is the density and $\Gamma = rU_\theta$ can be viewed as the circulation or the intensive (or specific) mean angular momentum. With this in mind it is of interest to investigate how the transport budget for Γ is balanced within the yz -plane in order to shed some light on the occurrence of the counter-rotating core. A balance equation for Γ , if we neglect viscous diffusion and $\partial \overline{u' u_\theta} / \partial x$, can be written as

$$U \frac{\partial \Gamma}{\partial x} + U_r \frac{\partial \Gamma}{\partial r} + \frac{1}{r} \frac{\partial}{\partial r} (r^2 \overline{u'_\theta u'_r}) = 0 \quad (6)$$

The first two terms are streamwise and radial advection of Γ , respectively, whereas the last term is transport through the cross stream Reynolds shear stress. We use the LDV data to analyze the different terms in this equation. The radial and streamwise variation of $\Gamma/(RV_w)$ is depicted in Fig. 6. Γ spreads radially outward very fast as it is advected downstream. It is apparent from Fig. 6 that the core of the jet (say $r/D < 0.3$) is a region of very low mean angular momentum and the latter keeps decreasing downstream until it eventually changes sign.

In the swirling jet, turbulence is efficient in transporting angular momentum radially outwards. Moreover, because the Reynolds shear stress $\overline{u'_\theta u'_r}$ is greater or equal to zero

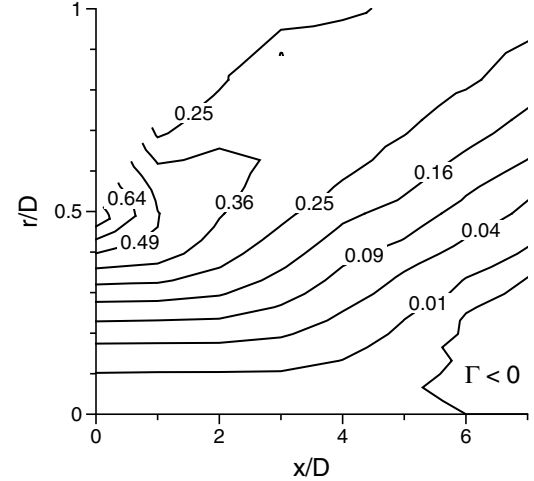


Fig. 6. Contours of intensive mean angular momentum. The contour levels are non-uniformly spaced as a function of $(\Gamma/(RV_w))^2$.

for all radial positions (Fig. 5), radial turbulent transport of Γ is directed outwards everywhere in the jet.

Consider an infinitesimal control volume (ICV) in the jet. A gain (loss) of Γ in the ICV is represented by a term of negative (positive) value in Eq. (6). Fig. 7 presents a budget of Γ at $x/D = 6$, a position where a counter-rotating core is present roughly between $r/D = 0$ and 0.25 . In the region represented in Fig. 7, streamwise advection leads everywhere to a gain of Γ in an ICV, while radial turbulent transport leads to a loss of Γ . Note that further outwards, radial turbulent transport has to eventually correspond to a gain since:

$$\frac{\partial}{\partial r} (r^2 \overline{u'_\theta u'_r}) < 0 \text{ for large } r \quad (7)$$

As can be seen in Fig. 7 the balance is not fulfilled in the outer part mainly because of the high uncertainties in

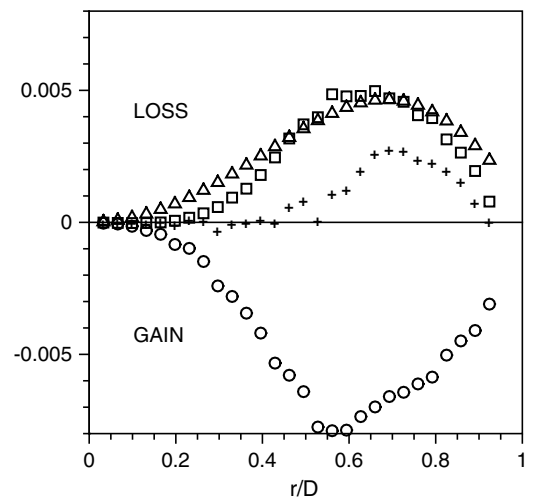


Fig. 7. Budget of mean angular momentum at $x/D = 6$. The terms are normalized with D and U_b . Streamwise advection (\circ), radial advection (\square), radial turbulent transport (\triangle), sum of all the terms ($+$).

$\partial\Gamma/\partial x$. The Γ data is too far apart in the streamwise direction to capture accurately the variations of Γ in the jet outer part.

Fig. 8 presents the same budget but now only in the core region. In this region, the loss of Γ due to turbulent transport is greater than the gain due to streamwise advection. Consequently, radial advection of Γ becomes negative (gain of Γ) while it was always positive upstream. The core region therefore starts to counter-rotate since

$$U_r \frac{\partial\Gamma}{\partial r} < 0 \Rightarrow \frac{\partial U_\theta}{\partial r} < 0 \Rightarrow U_\theta < 0 \quad (U_\theta = 0 \text{ at } r = 0) \quad (8)$$

If the swirling jet was laminar, streamwise and radial advections would always balance each other and counter-rotation would be impossible. Counter-rotation exists in a turbulent swirling jet because of the strong radial turbulent transport of mean angular momentum. If this also occurs in swirling jets which are generated in a different manner as compared to a long axially rotating pipe flow is at present an open question.

3.4. Instantaneous fields

By analysing the time and space resolved data from the stereoscopic PIV measurements and LES it is possible to capture the evolution of the flow and its structures. The figures presented next form a very limited selection of snapshots (combined vector/contour plots) taken from long sequences of time-resolved data. The discussion below is based on viewing videos of these long sequences of snapshots.

The LES database is used first to investigate the coherent structures at the pipe exit. It is important to stress that due to the presumed sensitivity of this flow to small changes in the inflow conditions, the instability mechanisms and the vortical structures present in the LES simu-

lations may differ slightly from those of the experiment. They are however expected to be qualitatively similar. Vortical structures are visualized using a criteria based on the second largest eigenvalue of the second invariant of the velocity derivative tensor, λ_2 , proposed by Jeong and Hussain (1995). In the following figures vortices correspond to a region where λ_2 is negative.

Fig. 9 shows a 3D visualization of the instantaneous vortical structures using λ_2 iso-surfaces for $x/D < 1.6$. Note that the axis box shown is for visual aid only and does not represent the actual computational box. The helical instability is seen to be dominant at the jet exit and it leads to the formation of large-scale helix-shape vortical structures. These structures most frequently appear in a double-helix, as in Fig. 9, or triple-helix configuration spatially revolving around the jet axis at a distance $\approx 0.4D$ and in the opposite direction compared to the rotation of the flow. These helical vortices are probably the result of the roll-up of helical waves corresponding to modes $m = 2$ and 3 . Fig. 10 illustrates that a quadruple-helix configuration (four vortices) also occurs sporadically. At around $x/D = 1.5$, the helical vortices occasionally merge into a single vortex ring as shown in Fig. 10.

Figs. 11 and 12 show that past $x/D = 2$, the large-scale vortices may become larger in diameter and more intense but also less organized. In Fig. 12, a constant advection velocity of $0.6U_b$ was removed in order to visualize the vortices. Smaller vortical structures are found further downstream, $x/D > 8$. They tend to be inclined in the azimuthal–axial plane probably due to the action of the azimuthal shear. Fig. 12 also shows that starting around $x/D = 4$, the high-speed core starts to move away from the axis. From iso-surfaces of the streamwise velocity (not shown here) it is found that the shape of the high-speed core is quite irregular and seldom resembles a helix. It rapidly changes shape and position with no apparent preferred direction of motion.

The time-resolved PIV instantaneous fields will now serve to establish a comparison between the non-swirling and swirling jets in the region around $x/D = 6$, where counter-rotation in the mean of the jet core exists in the swirling case. Clearly the first impression from viewing the videos of the PIV instantaneous velocity fields in the yz -plane at $x/D = 6$ is that the swirling jet contains much stronger large-scale motions than the non-swirling jet. A comparison of the $v-w$ vector plots shown in Figs. 13a and b illustrates this difference. Large sweeping motions that contribute significantly to $u'_\theta u'_r$ are frequent in the swirling jet while they do not occur at such a scale and strength in the non-swirling jet. Such motions appear frequently in the form of coherent bands (in the yz -plane) the size of the jet diameter. As a result, the side views of the flow (xz -plane) show quite frequently large vertical or V-shaped bands of v of the same sign, as seen in Fig. 14. Fig. 15 shows that a similar behaviour is found in the LES results. Note that U_θ is everywhere smaller than $0.07U_b$ at $x/D = 6$ (see Fig. 3). The mean swirling motion is therefore small com-

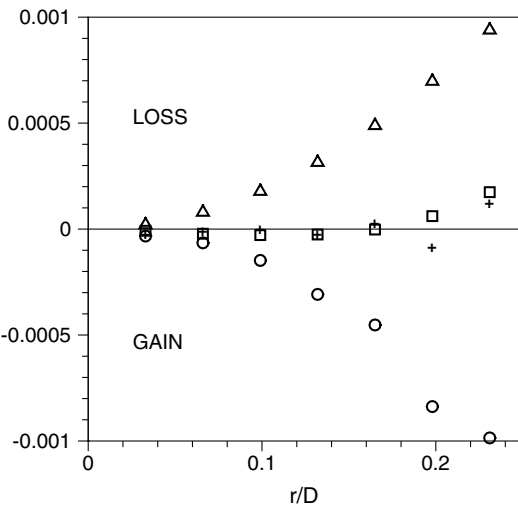


Fig. 8. Budget of mean angular momentum in the core region at $x/D = 6$. Symbols as in Fig. 7.

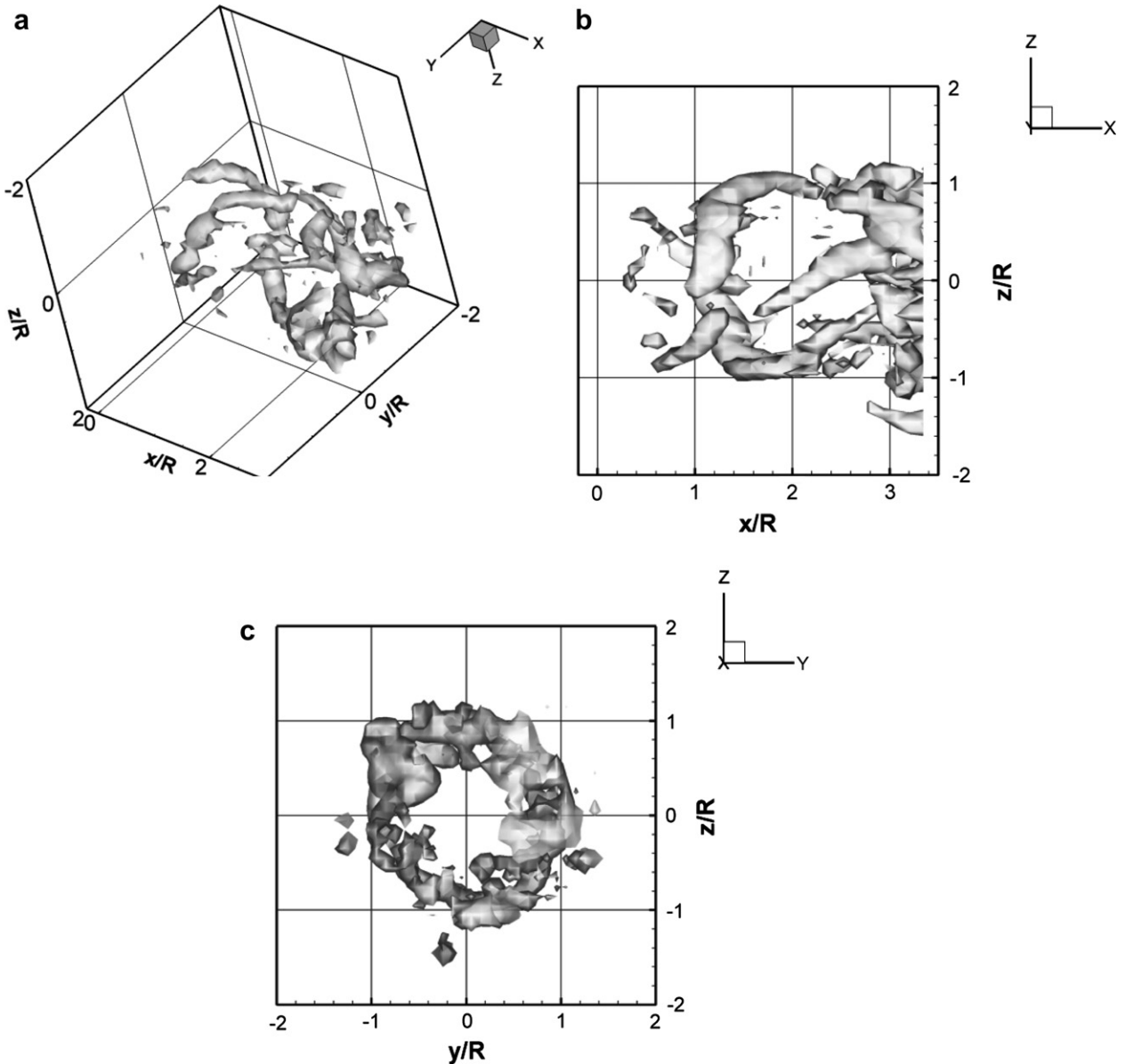


Fig. 9. LES snapshot of the instantaneous vortical structures in the swirling jet using λ_2 iso-surfaces. Only region $x/R < 3.2$ is shown to help visualize the initial helix-shape structures. (a) perspective view, (b) side view, (c) end view looking downstream.

pared to the sweeping motions shown in Figs. 13b, 14 and 15.

In both PIV and LES fields, the large-scale sweeping motions around $x/D = 6$ are usually found near large-scale vortices which are most probably the broken and/or amalgamated remnants of the helical vortices previously discussed. As mentioned previously, the high-speed core of the jet tends to quickly shift, stretch and deform in an apparently chaotic fashion. Hence, the counter-rotating core region of the swirling jet seems to be affected mostly by the large sweeping motions. No other coherent pattern has been identified that would be specific to that flow region.

In the case of the non-swirling jet, vortical motions are the dominant feature observed in the yz -plane (PIV data

in the xz -plane is not available). The high-speed core of the jet does not meander like in the swirling jet flow. Streamwise vortices concentrated along a centered ring band are sometimes found (see Fig. 13a), where the radius of the ring is approximately equal to the pipe radius R . These vortices could be the remnants of streamwise braids generated upstream as secondary shear layer instabilities. The lack of regularity in the occurrence and the shape of these rings of streamwise vorticity may be reinforced by the fact that the initial conditions of the jet are those of a turbulent pipe flow, as opposed to a thin laminar shear layer in the case of a smooth contraction jet flow. The rings of streamwise vortices were never observed in the swirling jet in neither the PIV nor the LES data. In the swirling jet, streamwise or quasi-streamwise vortices are located

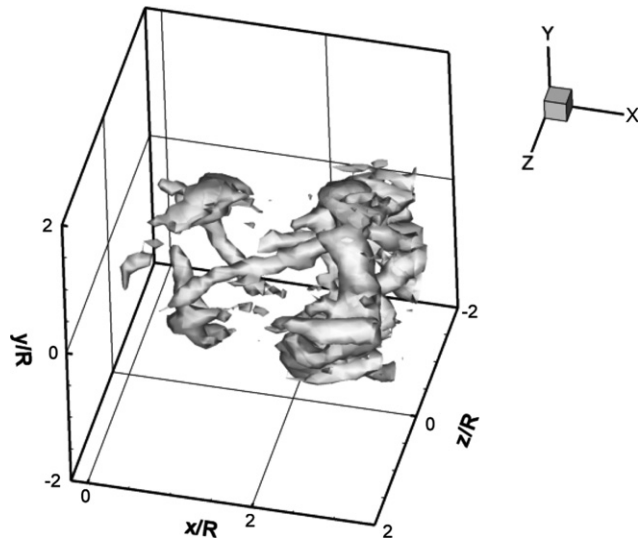


Fig. 10. LES snapshot of the instantaneous vortical structures in the swirling jet using λ_2 iso-surfaces. Only region $x/R < 3.2$ is shown to help visualize the vortex ring.

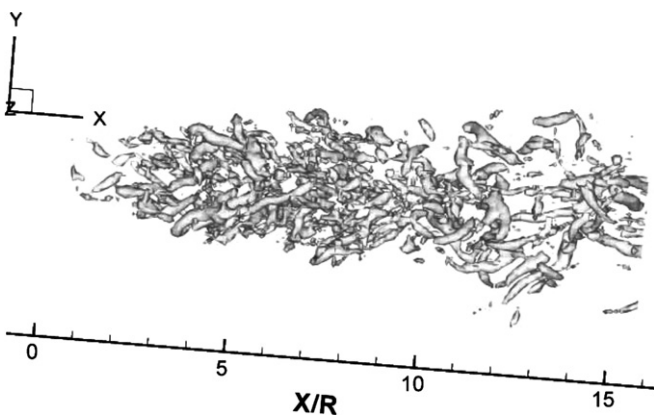


Fig. 11. LES Snapshot of the instantaneous vortical structures in the swirling jet using λ_2 iso-surfaces. Same field as Fig. 9.

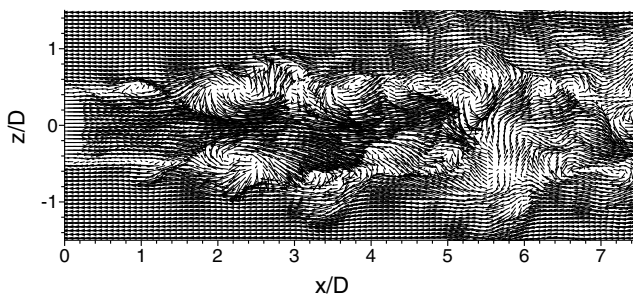


Fig. 12. LES instantaneous velocity field of the swirling jet in xz -plane at $y = 0$. Galilean decomposition with $U_c = 0.6U_b$.

everywhere in the jet in a more random fashion. They are however more present in and around the highly deformed jet core as is the case in Fig. 13b, where the high-speed core forms a large diagonal band. The large-scale streamwise vortices are typically of the same size and strength in both

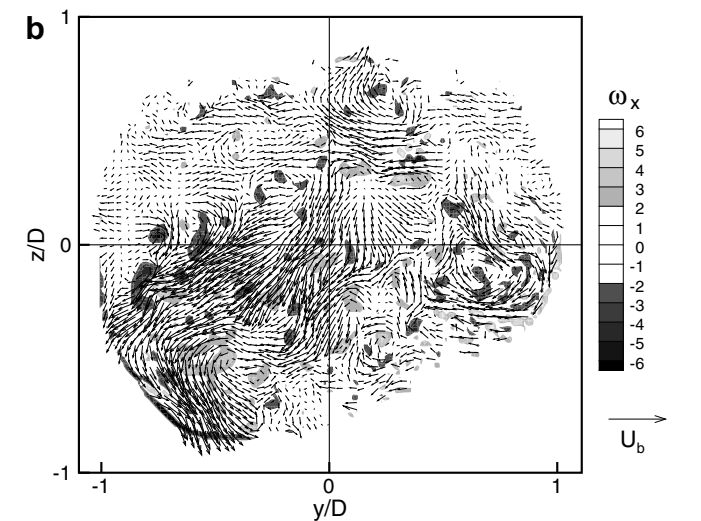
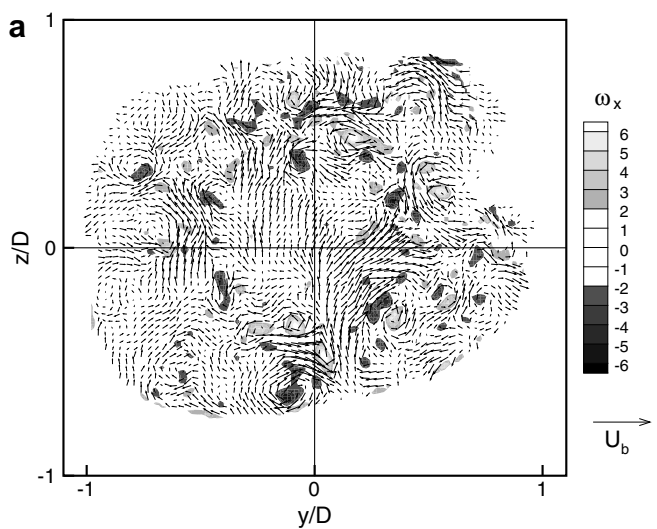


Fig. 13. PIV instantaneous velocity field at $x/D = 6$ and contours of streamwise vorticity with (a) $S = 0$ and (b) $S = 0.43$. Only one vector out of 4 is shown for clarity.

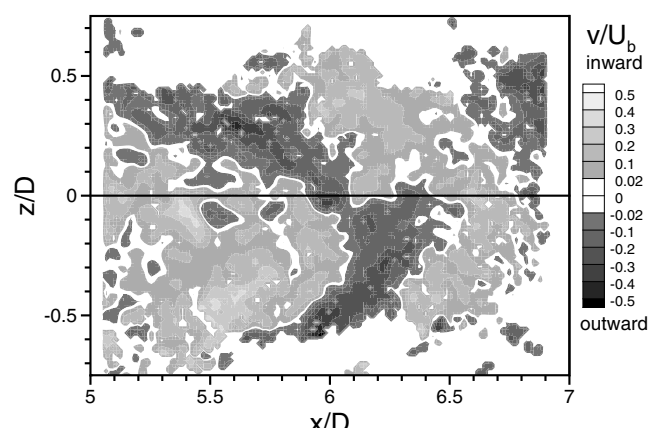


Fig. 14. PIV instantaneous contours of v in xz -plane at $y = 0$. $S = 0.43$.

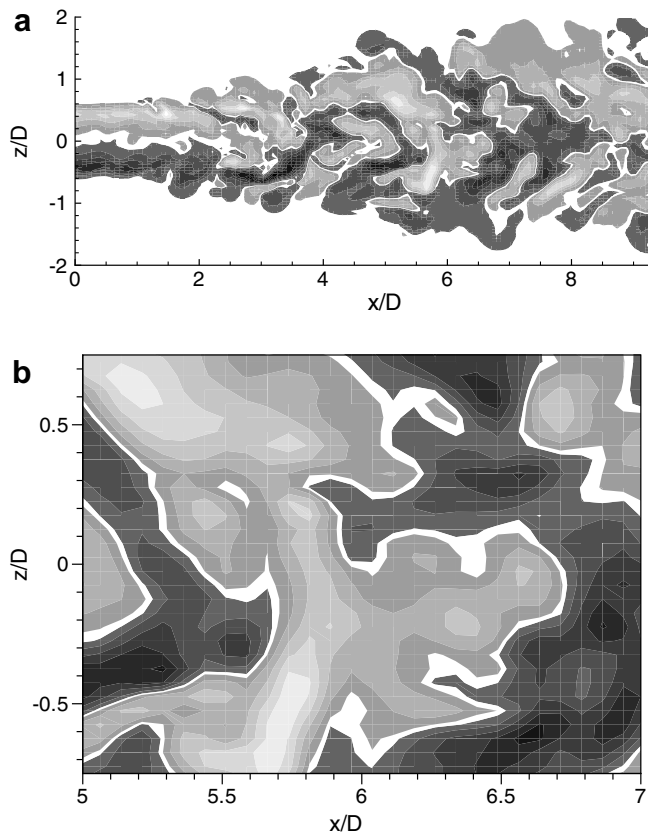


Fig. 15. LES instantaneous contours of v in xz -plane at $y = 0$. $S \approx 0.5$. (a) extended view, (b) close-up view similar to Fig. 14. Same contour levels as in Fig. 14.

the non-swirling and swirling jets. In the swirling jet, they are smaller than the large sweeping motions previously discussed and they can even be imbedded in them (Fig. 13b).

4. Conclusions

Experiments and large-eddy simulations have been carried out to study the near-field of a turbulent round jet with moderate swirl generated by a fully developed, axially rotating pipe flow. The flow statistics obtained from LES, LDV and time-resolved stereoscopic PIV measurements are compared and show a good agreement. The comparisons between the PIV and LDV measurements are particularly convincing. We have presented PIV data for all six Reynolds stress components for turbulent jets with and without swirl at $x/D = 6$. It is clear from these results that the swirl increases the turbulence intensities in the jet significantly. The budget for the angular momentum shows that the radial turbulent transport of mean angular momentum is important in the jet axis region and consequently causes a mean counter-rotation of the jet core.

The large-eddy simulations reveal that the flow at the pipe exit is dominated by helical instabilities leading to large-scale vortical structures in either double, triple or even quadruple-helix configuration. The vortices are occa-

sionally found to merge into a single vortex ring. All large-scale vortical structures rapidly break down and/or amalgamate after two jet diameters. In the process, they generally tend to become larger in diameter and more intense but also much less organized. Smaller vortical structures are found further downstream after eight jet diameters. They are usually inclined in the azimuthal–axial plane probably due to the action of the azimuthal shear.

Both time-resolved PIV and LES data show that the swirling jet at six jet diameters is dominated by strong, large-scale sweeping motions that are not present at such a scale and strength in the non-swirling jet. The strong sweeping motions frequently come together with a waviness of the jet core. Under their presence, the high-speed core of the jet tends to quickly shift, stretch and deform. These sweeping motions are often linked to the presence of large-scale azimuthal vortices. The latter are probably the remnants of the helical vortices formed upstream by the shear layer instabilities.

Counter-rotation in the mean of the core of the swirling jet was not found to be due to turbulent structures specific to the core region. It appears to be simply due to the fact that the large-scale turbulent motions, which lead to strong $u'_\theta u'_r$, are efficient in transporting mean angular momentum radially outward. Due to the highly turbulent nature of the flow, further insight on the coherent structures can only be gained with the help of analytical tools that clearly isolate the coherent structures from the smaller scale fluctuations, tools such as proper orthogonal decomposition (POD). A detailed POD study of the PIV and LES databases is currently underway.

Acknowledgements

The development of the rotating pipe facility and most of the measurements were sponsored by STEM, the Swedish Energy Agency. The PIV system was acquired through a generous grant from the Knut and Alice Wallenberg foundation. Part of this work was carried out when Y. Maciel was on a research visit to KTH in the summer of 2006, which was partly sponsored through STINT, The Swedish Foundation for International Cooperation in Research and Higher Education. Y. Maciel also gratefully acknowledges the financial support provided by NSERC of Canada. The routine for generating the seemingly turbulent inflow boundary conditions for the large-eddy simulations was kindly provided by Markus Klein. The computations were run on the Lund University computing facilities (LUNARC).

References

- Ahlman, D.A., Brethouwer, G., Johansson, A.V., 2007. Direct numerical simulation of a plane turbulent wall-jet including scalar mixing. *Phys. Fluids* 19, 065102.
- Boersma, B.J., Brethouwer, G., Nieuwstadt, F.T.M., 1998. A numerical investigation on the effect of the inflow conditions on the self-similar region of a round jet. *Phys. Fluids* 10 (4), 899–909.

Crow, S.C., Champagne, F.H., 1971. Orderly structure in jet turbulence. *J. Fluid Mech.* 48, 547–591.

da Silva, C.B., Métais, O., 2002. Vortex control of bifurcating jets: a numerical study. *Phys. Fluids* 14 (11), 3798–3819.

Dimotakis, P.E., Miike-Lye, R.C., Papantoniou, D.A., 1983. Structure and dynamics of round turbulent jets. *Phys. Fluids* 26 (11), 3185–3192.

Ducros, F., Comte, P., Lesieur, M., 1996. Large-eddy simulation of transition to turbulence in a boundary layer spatially developing over a flat plate. *J. Fluid Mech.* 326, 1–36.

Duwig, C., Fuchs, L., Griebel, P., Siewert, P., Boschek, E., 2007. Study of a confined turbulent jet: influence of combustion and pressure on the flow. *AIAA J.* 45 (3), 624–639.

Duwig, C., Fureby, C., 2007. Large eddy simulation of unsteady lean stratified premixed combustion. *Combust. Flame* 151 (1–2), 85–103.

Duwig, C., Salewski, M., Fuchs, L., 2008. Large eddy simulation of a turbulent flow past two symmetric backward-facing steps: a sensitivity analysis. *AIAA J.* 46 (2), 408–419.

Facciolo, L., 2006. A study on axially rotating pipe and swirling jet flows. Ph.D. Thesis, Royal Institute of Technology, Stockholm, Sweden.

Facciolo, L., Tillmark, N., Talamelli, A., Alfredsson, P.H., 2007. A study of swirling turbulent pipe and jet flows. *Phys. Fluids* 19, 035105.

Gullbrand, J., Bai, X.S., Fuchs, L., 2001. High-order Cartesian grid method for calculation of incompressible turbulent flows. *Int. J. Numer. Meth. Fluids* 36 (6), 687–709.

Ho, C.M., Huerre, P., 1984. Perturbed free shear layers. *Annu. Rev. Fluid Mech.* 16, 365–422.

Hu, G.-H., Sun, D.-J., Yin, X.-Y., 2001. A numerical study of dynamics of a temporally evolving swirling jet. *Phys. Fluids* 13 (14), 951–965.

Jeong, J., Hussain, F., 1995. On the identification of a vortex. *J. Fluid Mech.* 285, 69–94.

Klein, M., Sadiki, A., Janicka, J., 2003. A digital filter based generation of inflow data for spatially developing direct numerical or large eddy simulations. *J. Comp. Phys.* 186, 652–665.

Loiseleur, T., Chomaz, J.M., 2003. Breaking of rotational symmetry in a swirling jet experiment. *Phys. Fluids* 15 (2), 511–523.

Martin, J.E., Meiburg, E., 1994. On the stability of the swirling jet shear layer. *Phys. Fluids* 6 (2), 424–426.

Martin, J.E., Meiburg, E., 1998. The growth and nonlinear evolution of helical perturbations in a swirling jet model. *Eur. J. Mech. B/Fluids* 17, 639–651.

McIlwain, S., Pollard, A., 2002. Large eddy simulation of the effects of mild swirl on the near field of a round free jet. *Phys. Fluids* 14 (2), 653–661.

Mi, J., Nobes, D.S., Nathan, G.J., 2001. Influence of jet exit conditions on the passive scalar field of an axisymmetric free jet. *J. Fluid Mech.* 432, 91–125.

Michalke, A., 1984. Survey on jet instability theory. *Prog. Aerosp. Sci.* 21, 159–199.

Olsson, M., Fuchs, L., 1996. Large eddy simulation of the proximal region of a spatially developing circular jet. *Phys. Fluids* 8 (8), 2125–2137.

Panda, J., McLaughlin, D.K., 1994. Experiments on the instabilities of a swirling jet. *Phys. Fluids* 6 (1), 263–276.

Russ, S., Strykowski, P.J., 1994. Turbulent structure and entrainment in heated jets: the effect of initial conditions. *Phys. Fluids A* 5 (12), 3216–3225.

Sagaut, P., 2001. Large Eddy Simulation for Incompressible Flows. Springer Verlag.

Xu, G., Antonia, R.A., 2002. Effect of different initial conditions on a turbulent round free jet. *Exp. Fluids* 33, 677–683.